



# CHORUS

This is the accepted manuscript made available via CHORUS. The article has been published as:

## Theoretical and experimental study of second harmonic generation from the surface of the topological insulator $\text{Bi}_2\text{Se}_3$

J. W. McIver, D. Hsieh, S. G. Drapcho, D. H. Torchinsky, D. R. Gardner, Y. S. Lee, and N. Gedik

Phys. Rev. B **86**, 035327 — Published 27 July 2012

DOI: [10.1103/PhysRevB.86.035327](https://doi.org/10.1103/PhysRevB.86.035327)

# A theoretical and experimental study of second harmonic generation from the surface of the topological insulator $\text{Bi}_2\text{Se}_3$

J. W. McIver,<sup>1,2</sup> D. Hsieh,<sup>1</sup> S.G. Drapcho,<sup>1</sup> D. H. Torchinsky,<sup>1</sup> D. R. Gardner,<sup>1</sup> Y. S. Lee,<sup>1</sup> and N. Gedik<sup>1</sup>

<sup>1</sup>*Department of Physics, Massachusetts Institute of Technology, Cambridge, MA 02139, USA*

<sup>2</sup>*Department of Physics, Harvard University, Cambridge, MA 02138, USA*

(Dated: June 28, 2012)

We develop a theoretical model that describes the second harmonic generation of light from the surface of the topological insulator  $\text{Bi}_2\text{Se}_3$  and experimentally demonstrate that the technique is sensitive to the surface electrons. By performing a crystal symmetry analysis of  $\text{Bi}_2\text{Se}_3(111)$  we determine the nonlinear electric susceptibility tensor elements that give rise to second harmonic generation. Using these results, we present a phenomenological model that shows that the relative magnitudes of these tensor elements can be determined by measuring the polarization and intensity of the radiated second harmonic light as a function of the in-plane crystal orientation and incident laser polarization. We describe optical techniques capable of isolating second harmonic light and using these techniques we measure the first-order linear optical and second-order nonlinear optical responses as a function of crystal orientation and laser polarization on bulk single crystals of  $\text{Bi}_2\text{Se}_3(111)$ . The experimental results are consistent with our theoretical description. By comparing the data to our theoretical model we determine that a portion of the measured second harmonic light originates from the accumulation region of  $\text{Bi}_2\text{Se}_3(111)$ , which we confirm by performing surface doping-dependent studies. Our results show that second harmonic generation is a promising tool for spectroscopic studies of topological surfaces and buried interfaces.

PACS numbers:

## I. INTRODUCTION

The three-dimensional (3D) topological insulator [1–3] is a new quantum phase of matter that is characterized by an inverted bulk band gap and topologically protected surface states [4, 5], which have been comprehensively imaged by both photoemission [4–8] and tunneling [9, 10] spectroscopies. The electrical response properties of an isolated surface are predicted to be highly novel, including protection against backscattering from non-magnetic impurities [1–3] and a switchable spin-polarized electrical current [11–13]. When interfaced with certain topologically trivial materials, the surface states are predicted to evolve into new broken symmetry electronic phases that may exhibit topological superconductivity [2] and an anomalous half-integer quantum Hall effect [2, 14], which have been proposed as media to search for Majorana fermions [1, 2] and charge fractionalization in three-dimensions [15]. Owing to these exciting theoretical proposals, the recent discovery of 3D topological insulator phases in  $\text{Bi}_{1-x}\text{Sb}_x$  [4, 5],  $\text{Bi}_2\text{Se}_3$  [6, 16] and related materials [7, 16, 17] has generated great interest to measure their symmetry and electrical properties at an isolated surface or buried interface. However, a major experimental obstacle has been the high density of mobile electrons in the bulk of these materials, which can overwhelm the surface or interface electrical responses. Although transport results on electrically gated samples show evidence for surface carrier modulation [18–20], the contributions to the electrical response from carriers on different surfaces and in the bulk are difficult to separate and require highly insulating samples. Moreover, contacts and gates deposited on the surface may perturb the intrinsic surface

electronic structure [21].

Optical probes have been proposed as a contact free alternative that can be focused onto a single surface [11, 14, 22, 23]. However, most experiments to date have been limited to the linear optical regime, which has been shown to be dominated by the bulk electrical response [24–26] except in the limit of very thin samples [27, 28]. Recently, nonlinear second harmonic generation (SHG) of light from bulk single crystals of  $\text{Bi}_2\text{Se}_3$  was shown to be highly sensitive to electrons confined to the surface and accumulation region [29, 30]. The underlying principle for this surface sensitivity is that SHG is predominantly generated where inversion symmetry is broken [31], which only occurs at the surface of the bulk inversion-symmetric  $\text{Bi}_2\text{Se}_3$  and in the accumulation region where the band-bending induced electric field breaks inversion symmetry.

In this work, we develop a theoretical model that describes the SHG intensity from  $\text{Bi}_2\text{Se}_3$  in terms of the second- and third-order nonlinear electric susceptibilities. By performing a symmetry analysis of  $\text{Bi}_2\text{Se}_3$  we identify the susceptibility tensor elements that contribute to SHG and show that their relative magnitudes can be determined by measuring the intensity and polarization of the emitted SHG as a function of crystal orientation and incident laser polarization. To test the model, bulk single crystals of  $\text{Bi}_2\text{Se}_3$  were grown, characterized and SHG experiments were performed using both linear and circularly polarized laser light. The experimental results are described well by our theoretical model. Application of the model to our data shows that approximately half of the SHG from  $\text{Bi}_2\text{Se}_3$  at long times after cleaving in air originates from the surface while the rest originates from the accumulation region. A surface doping-dependent

study verifies that the SHG intensity depends on the surface carrier concentration, which shows that SHG can be used to optically probe changes in the surface Fermi level.

The paper is organized as follows: In section II, we perform a crystal symmetry analysis on  $\text{Bi}_2\text{Se}_3$  to determine the nonlinear susceptibility tensor elements that give rise to SHG. We then present a phenomenological model that describes how these tensor elements are manifested in the SHG intensity and polarization. In section III, we first detail the SHG growth procedures, sample characterization results, and SHG experimental methods used to isolate the surface response. We then report the measured SHG intensity and polarization and compare the results to the theoretical model developed in section II. Finally, we report the effects of surface doping on SHG and investigate circular dichroism SHG. A summary is provided in section IV, followed by the appendix in section V.

## II. THEORETICAL BACKGROUND

This section is organized into two parts. In section II.A, we determine the susceptibility tensor elements that give rise to SHG in  $\text{Bi}_2\text{Se}_3$  by performing a crystal symmetry analysis. In section II.B, we present a phenomenological model that describes the intensity and polarization of second harmonic light generated from  $\text{Bi}_2\text{Se}_3$  using these tensor elements.

### A. Symmetry analysis and electric susceptibility tensors of $\text{Bi}_2\text{Se}_3(111)$

The electrical response of a material is described by susceptibility tensors  $\chi^{(n)}$  that relate the electric polarization of the material  $\vec{P}$  to the applied electric field  $\vec{E}$  through the power-series expansion [31]

$$P_i = \chi_{ij}^{(1)} E_j + \chi_{ijk}^{(2)} E_j E_k + \chi_{ijkl}^{(3)} E_j E_k E_l + \dots \quad (1)$$

where the indices run through spatial coordinates. The susceptibility tensor elements of each  $\chi^{(n)}$  can be determined by performing a crystal symmetry analysis. The bulk crystal structure of  $\text{Bi}_2\text{Se}_3(111)$ , which belongs to space group  $D_{3d}^5$ , remains invariant under a group of symmetry operations  $T$ . These consist of (i) rotation along the (111) axis by  $0^\circ$ ,  $120^\circ$  and  $240^\circ$ , (ii) mirror reflection under planes  $a$ ,  $b$  and  $c$  [Fig.1], and (iii) inversion symmetry about some center of inversion. Because  $\chi^{(n)}$  must obey the same symmetries as the crystal, they must be invariant under the same group of symmetry operations that bring  $\chi^{(n)}$  to  $\chi^{(n)'}$ , which is given by [31]

$$\chi_{i_1 i_2 \dots i_{n+1}}^{(n)'} = \sum_{j_1, j_2 \dots j_{n+1}} T_{i_1 j_1} T_{i_2 j_2} \dots T_{i_{n+1} j_{n+1}} \chi_{j_1 j_2 \dots j_{n+1}}^{(n)} \quad (2)$$

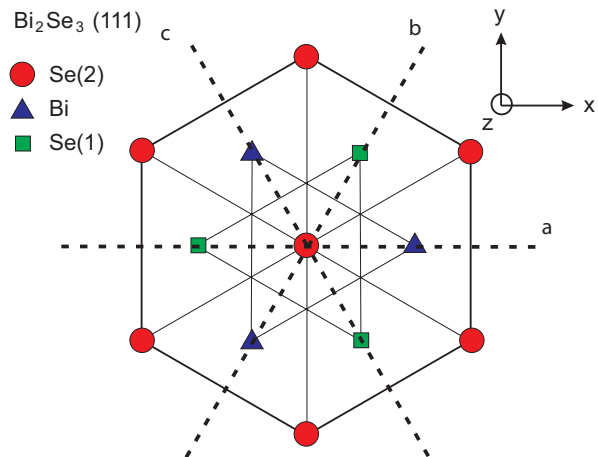


FIG. 1: Schematic of the  $\text{Bi}_2\text{Se}_3$  crystal coordinate system showing the  $C_{3v}$  symmetry of the (111) cleaved surface. The bulk  $D_{3d}^5$  symmetry is given by the addition of inversion symmetry. The three-fold rotation symmetry and the three planes of mirror symmetry ( $a$ ,  $b$  and  $c$ ) are illustrated. The topmost, second and third atomic layers are Se(2), Bi and Se(1) respectively. The beam coordinate system is shown in the top right.

Under such transformations, the crystal symmetry greatly reduces the number of non-zero independent components of  $\chi^{(n)}$ .

We first examine the first-order response characterized by  $\chi^{(1)}$  in eq.(1). Because  $\chi^{(1)}$  is an even rank tensor and  $P_i$  and  $E_j$  are both odd under the operation of inversion, a first-order response is permitted regardless of whether or not crystal inversion symmetry is present. Therefore, the linear optical response can include contributions from both the inversion symmetric bulk of  $\text{Bi}_2\text{Se}_3$  as well as from the (111) surface where inversion symmetry is necessarily broken [31]. The individual tensor elements can be found by transforming  $\chi^{(1)}$  under the rotation, mirror and inversion symmetry operations that characterize bulk  $\text{Bi}_2\text{Se}_3$  via eq.(2) and equating the resulting tensors. Using this procedure, we find that  $\chi^{(1)}$  assumes the form

$$\chi^{(1)} = \begin{pmatrix} \chi_{11}^{(1)} & 0 & 0 \\ 0 & \chi_{22}^{(1)} & 0 \\ 0 & 0 & \chi_{33}^{(1)} \end{pmatrix} \quad (3)$$

where  $\chi_{11}^{(1)} = \chi_{22}^{(1)}$ , and  $\chi_{33}^{(1)}$  are scalars [32]. This yields an isotropic first-order electrical response in the (111) plane. Although both bulk and surface contribute to this response, the bulk contribution usually dominates. This is because the linear optical response is an integrated measure over the depth that light penetrates into the sample, which is typically on the order of hundreds of atomic layers.

We now analyze how the  $\text{Bi}_2\text{Se}_3(111)$  crystal symmetry affects the second-order dipolar response  $\chi^{(2)}$ . From

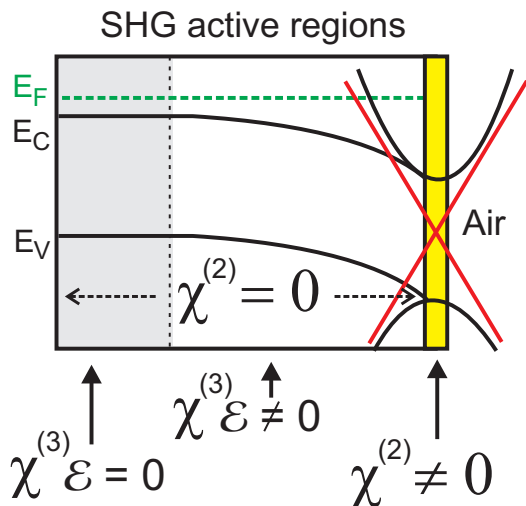


FIG. 2: Schematic of the energy evolution of the bulk conduction band minimum ( $E_C$ ) and bulk valence band maximum ( $E_V$ ) relative to the Fermi level ( $E_F$ ) as a function of distance to the air covered surface. The SHG active regions are where  $\chi^{(2)} + \chi^{(3)}\mathcal{E} \neq 0$ , which represent the surface (yellow) and accumulation region (white) contributions respectively.

eq.(2) we see that all of the components of odd rank tensors must vanish under the inversion operator  $T_{ij} = -\delta_{ij}$  because each component is mapped to the negative of itself. Therefore, all 27 components of  $\chi^{(2)}$  must be zero in the inversion symmetric bulk of  $\text{Bi}_2\text{Se}_3$ . However, at the cleaved (111) surface inversion symmetry is broken and the crystal symmetry is reduced to  $C_{3v}$  symmetry. In the case of  $\text{Bi}_2\text{Se}_3$ , cleavage occurs naturally between two Se layers that are Van der Waals bonded to expose large areas that are Se terminated [1–3]. Owing to this lack of inversion symmetry at the surface, non-vanishing components of odd rank tensors such as  $\chi^{(2)}$  are permitted to exist. The individual  $\chi^{(2)}$  tensor components for  $\text{Bi}_2\text{Se}_3$  are shown in the appendix. In section II.B we show how these tensor elements are manifested in the SHG intensity and polarization as a function of the crystal orientation and incident laser polarization.

In addition to the surface  $\chi^{(2)}$  contribution, SHG can be generated by accumulation layer electrons. These are bulk electrons confined near the surface by a band-bending induced electric field  $\vec{\mathcal{E}}$  directed perpendicular to the surface. SHG is highly sensitive to a static electric field because it acts to break inversion symmetry over the accumulation region [Fig.2]. Electric-field induced SHG is commonly observed in the context of metal-electrolyte interfaces [33] and is theoretically described by a third-order process  $P_i(2\omega) = \chi_{ijkl}^{(3)}\mathcal{E}_j(\omega)E_k(\omega)E_l(0)$  that acts in addition to  $\chi^{(2)}$  [31, 33, 34]. Because  $\chi^{(3)}$  has the same symmetry constraints as  $\chi^{(2)}$ , the overall symmetry of the SHG intensity as a function of the crystal orientation must remain unchanged in the presence of  $\vec{\mathcal{E}}$  with each  $\chi^{(2)}$  tensor element simply being enhanced by the addition of a  $\chi^{(3)}\vec{\mathcal{E}}$  tensor element. The non-vanishing

$\chi^{(3)}$  tensor elements for  $\text{Bi}_2\text{Se}_3$  are determined in the appendix.

We note that there may also be higher multipole bulk contributions to SHG that can be finite even in inversion symmetric systems [31] and that will have the same symmetry properties as both the surface  $\chi^{(2)}$  and  $\chi^{(3)}$  tensors [32] shown above. The bulk electric quadrupole and magnetic dipole contributions are the dominant of these higher multipole susceptibilities, however they are generally suppressed relative to the dipolar susceptibilities by a factor of  $ka$ , where  $k$  is the wavevector of the incident light and  $a$  is a lattice constant [31]. In reflection measurements, the bulk contribution only comes from a layer within the optical penetration depth ( $\xi$ ) of the incident light, which we determine to be  $\sim 25$  nm at 795 nm (section III.A). The surface contribution will come from the entire depth  $d$  over which the surface wavefunctions penetrate into the bulk, which is of the order  $d \equiv \hbar v_f / \Delta \sim 10$  Å for states within the bulk-gap, and is much larger for states not in the bulk gap, where  $v_f$  is the Fermi velocity,  $\hbar$  is the reduced Planck’s constant, and  $\Delta$  is the bulk band gap energy. Therefore, the relative intensity of the surface to bulk second harmonic radiation is approximately  $|\frac{1}{ka} \frac{d}{\xi}|^2 = |\frac{7.95 \times 10^3 \text{Å}}{2\pi \times 2\text{Å}} \frac{10\text{Å}}{2.5 \times 10^2 \text{Å}}|^2 \sim 640$ . Indeed, measurements on other strong spin-orbit coupled materials, such as Au, in the regime where interband transitions dominate ( $\Delta < \hbar\omega$ ) have shown that these bulk contributions are greatly suppressed [35]. Bulk contributions have only been shown to be observable when  $\Delta > \hbar\omega$ , where the penetration depth of the light into the crystal is very deep [36]. All of our measurements were performed in the regime  $\Delta < \hbar\omega$  and we experimentally demonstrate in section III.C by varying the surface carrier density that these higher order bulk effects are indeed not dominant.

## B. Phenomenological model of surface SHG

In this section, we show how the intensity of second harmonic radiation is related to the nonlinear susceptibility tensors derived in section II.A. Our phenomenological model of surface SHG follows the convention developed by Mizrahi and Sipe (1988) [37], which builds on the earlier work of Heinz (1982) [38] and Bloembergen & Pershan (1962) [39]. The model assumes that the source of surface SHG is a thin electric dipole sheet confined to the surface. Following the notation used in ref. [37] for surface SHG from a thick crystal in the reflection geometry, the second harmonic intensity  $I(2\omega)$  is given by

$$I(2\omega) = A \times |\hat{e}_i(2\omega) (\chi_s)_{ijk} \hat{e}_j(\omega) \hat{e}_k(\omega)|^2 I(\omega)^2 \quad (4)$$

where  $A$  is a geometrical constant,  $\hat{e}(\omega)$  is the beam polarization of the incoming radiation field inside the crystal,  $\hat{e}(2\omega)$  is the beam polarization of the outgoing second harmonic radiation field inside the crystal,  $I(\omega)$  is the

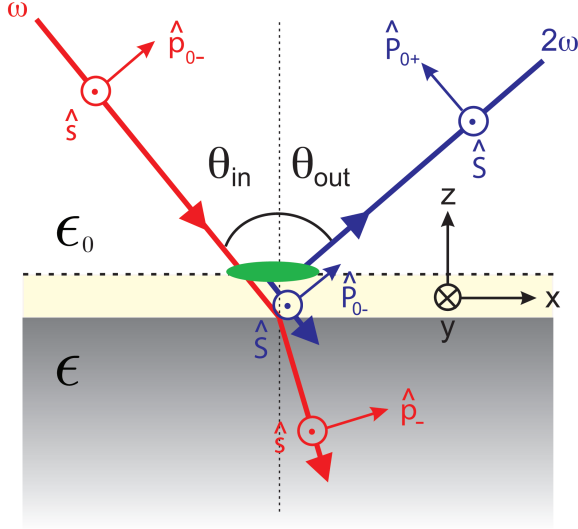


FIG. 3: Schematic of the incoming and outgoing laser beam geometry and polarizations. The polarization vectors of the fundamental and second harmonic beams are labeled by lower case and upper case letters respectively. The cream colored region at  $z = 0$  denotes the electric dipole sheet at the surface as described in ref. [37]. The interaction volume of the beams is demarcated by the green shaded region. The refracted fundamental beam is displaced downward and the fundamental and second harmonic beams are separated for visual clarity.

intensity of the incident beam,  $\chi_s$  is the complex surface nonlinear susceptibility tensor, and the indices run through  $x$ ,  $y$  and  $z$ . The polarization directions are defined in Fig.3. The incident unit polarization vector is given by

$$\hat{e}(\omega) = \frac{E_{in}^s}{|E_{in}|} t_{0m}^s \hat{s} + \frac{E_{in}^p}{|E_{in}|} t_{0m}^p \hat{p}_- \quad (5)$$

where  $E_{in}^{s,p}$  are the  $s$ - and  $p$ -polarized components of the incident electric field,  $t_{0m}^{s,p}$  are the complex Fresnel coefficients for transmission of the fundamental beam from air into the medium with electric permittivity  $\epsilon$ , and  $\hat{s}$ ,  $\hat{p}_-$  are the  $s$ - and  $p$ -polarization directions of the fundamental beam in the crystal. The outgoing second harmonic unit polarization vector is given by

$$\hat{e}(2\omega) = \frac{E_{out}^S}{|E_{out}|} (1 + R_{0m}^s) \hat{S} + \frac{E_{out}^P}{|E_{out}|} (\hat{P}_{0+} + R_{0m}^p \hat{P}_{0-}) \quad (6)$$

where  $E_{out}^{S,P}$  are the  $s$ - and  $p$ -polarized components of the outgoing second harmonic electric field,  $R_{0m}^{s,p}$  is the complex Fresnel coefficient for reflection of the second harmonic beam off of the bulk medium beneath the surface

electric dipole sheet [37],  $\hat{S}$  denotes the  $s$ -polarized direction of the reflected second harmonic light,  $\hat{P}_{0+}$  is the  $p$ -polarized component of second harmonic light that is reflected off the top surface of the dipole sheet, and  $\hat{P}_{0-}$  is the  $p$ -polarized component that reflects off the bulk medium after being generated at the surface.

In our model we assume that  $(\chi_s)_{ijk} = \chi_{ijk}^{(2)} + \chi_{ijkl}^{(3)} \mathcal{E}_l$  in eq.(4), which represents the combined surface plus accumulation region response. This is a simplification as the presence of a band-bending induced electric field  $\mathcal{E}$  will alter the index of refraction, and hence the Fresnel coefficients, as a function of depth into the bulk. However, accounting for this effect is beyond the scope of our work. In our calculation we let  $\mathcal{E}$  lie only along the  $z$  direction because the atomic layers must be equipotentials. The Fresnel coefficients at the fundamental and second harmonic frequency were calculated using the Fresnel equations [40], where for the complex indices of refraction  $\tilde{n} = n + ik$  we use  $\tilde{n}(\omega) = 5.46 + i2.57$  and  $\tilde{n}(2\omega) = 2.07 + i3.43$ , which we determine experimentally for our  $\text{Bi}_2\text{Se}_3$  samples in Section III.A. We assume  $\theta_{in} = \theta_{out} = 45^\circ$  based on our experimental configuration (Section III.A). Using these parameters in equations (4)–(6), we obtain expressions for the intensity of second harmonic radiation as a function of the in-plane crystal orientation angle  $\phi$  [Fig.1] under different linear polarization geometries and circular polarization geometries as follows:

$$\begin{aligned} I_{PP}(2\omega) &= B |(0.0012 + 0.0034i) c^{(3)} \\ &\quad + (0.076 - 0.038i) c^{(2)} \\ &\quad + (0.00030 - 0.0012i) c^{(4)} \\ &\quad - (0.0030 - 0.030i) c^{(1)} \cos(3\phi)|^2 \\ I_{SP}(2\omega) &= B |(0.045 - 0.027i) c^{(2)} \\ &\quad + (0.00013 - 0.018i) c^{(1)} \cos(3\phi)|^2 \\ I_{SS}(2\omega) &= B |(0.0019 + 0.014i) c^{(1)} \sin(3\phi)|^2 \\ I_{PS}(2\omega) &= B |(-0.00092 - 0.024i) c^{(1)} \sin(3\phi)|^2 \quad (7) \end{aligned}$$

and

### III. EXPERIMENTAL RESULTS AND DISCUSSION

$$\begin{aligned}
I_{RS}(2\omega) &= B |(0.0019 - 0.0011i) c^{(3)} \\
&\quad - (0.037 - 0.0031i) c^{(1)} \cos(3\phi) \\
&\quad + (0.0028 + 0.0378i) c^{(1)} \sin(3\phi)|^2 \\
I_{LS}(2\omega) &= B |(0.0019 - 0.0011i) c^{(3)} \\
&\quad - (0.037 - 0.0031i) c^{(1)} \cos(3\phi) \\
&\quad - (0.0028 + 0.0378i) c^{(1)} \sin(3\phi)|^2 \\
I_{RP}(2\omega) &= B |(-0.0012 - 0.0034i) c^{(3)} \\
&\quad - (0.032 - 0.010i) c^{(2)} \\
&\quad - (0.00026 - 0.0012i) c^{(4)} \\
&\quad + (0.0031 - 0.049i) c^{(1)} \cos(3\phi) \\
&\quad - (0.047 + 0.0025i) c^{(1)} \sin(3\phi)|^2 \\
I_{LP}(2\omega) &= B |(-0.0012 - 0.0034i) c^{(3)} \\
&\quad - (0.032 - 0.010i) c^{(2)} \\
&\quad - (0.00026 - 0.0012i) c^{(4)} \\
&\quad + (0.0031 - 0.049i) c^{(1)} \cos(3\phi) \\
&\quad + (0.047 + 0.0025i) c^{(1)} \sin(3\phi)|^2
\end{aligned} \tag{8}$$

where the subscripts for each  $I_{in-out}(2\omega)$  refer to the input fundamental and output second harmonic polarizations, and  $B = A \times I(\omega)^2$ . In the above equations,  $c^{(n)} = a^{(n)} + b^{(n)}$  where

$$\begin{aligned}
a^{(1)} &= \chi_{xxx} \\
a^{(2)} &= \chi_{zxx} \\
a^{(3)} &= 2 \chi_{xxz} \\
a^{(4)} &= \chi_{zzz}
\end{aligned} \tag{9}$$

represent the surface  $\chi^{(2)}$  SHG and

$$\begin{aligned}
b^{(1)} &= -\chi_{xyyz} \mathcal{E}_z \\
b^{(2)} &= \chi_{zxxz} \mathcal{E}_z \\
b^{(3)} &= (\chi_{xzzz} + \chi_{xxzz}) \mathcal{E}_z \\
b^{(4)} &= \chi_{zzzz} \mathcal{E}_z
\end{aligned} \tag{10}$$

represent the electric field-induced SHG over the accumulation region due to  $\chi^{(3)} \mathcal{E}$ . The relative magnitudes of  $c^{(n)}$  can be experimentally determined by measuring  $I(2\omega)$  as a function of in-plane crystal orientation angle  $\phi$  and laser polarization. The relative contributions of  $a^{(n)}$  and  $b^{(n)}$  can then be determined by varying the surface carrier density. The experimental results are shown in section III.

This section is organized into five parts. In section III.A we report our  $\text{Bi}_2\text{Se}_3$  growth procedure, sample characterization results and describe the optical techniques used to isolate second harmonic light. In section III.B we characterize the first-order linear optical response of our  $\text{Bi}_2\text{Se}_3$  material, then the second-order nonlinear optical response in section III.C. In section III.D we report how changing the surface carrier concentration through molecular doping affects the SHG signal. Finally, in section III.E we characterize the intrinsic SHG circular dichroism from  $\text{Bi}_2\text{Se}_3$ .

#### A. Methods and sample characterization

In this work, samples of  $\text{Bi}_2\text{Se}_3$  were lightly hole-doped by substituting As into the Se planes to reduce the bulk carrier concentration [19, 41], although they remain electrically conducting. Single crystal  $\text{Bi}_{2-x}\text{As}_x\text{Se}_3$  was grown by melting a 10 g stoichiometric mixture of Bi and Se shot with trace amounts of As powder ( $x=0.00129$ ) in an evacuated quartz tube at  $850^\circ\text{C}$ . After 12 hours at this temperature, the mixture was cooled to  $720^\circ\text{C}$  over two hours, then slowly cooled to  $650^\circ\text{C}$  over two days. The batch was annealed at  $650^\circ\text{C}$  for two more days then furnace cooled to room temperature.

After growth, the crystal orientation was determined by X-ray diffraction using a Bruker D8 diffractometer with Cu  $K\alpha$  radiation ( $\lambda = 1.54\text{\AA}$ ) and a two-dimensional area detector. The real ( $n$ ) and imaginary ( $k$ ) parts of the index of refraction were determined between 350nm and 820nm by performing spectroscopic ellipsometry measurements using a Sopra GES 5 Spectroscopic Ellipsometer and accompanying WinElli software [Fig.4(a)]. The optical penetration depth, which is given by  $\xi = \lambda/4\pi k$  [42], is shown in Fig.4(b). We find that  $\xi \sim 25$  nm at  $\lambda=795$  nm, which is the fundamental wavelength used in all SHG measurements. Samples were characterized by Fourier Transform Infrared Spectroscopy (FTIR) using a Nicolet Magna 860 FTIR Spectrometer [Fig.4(b) inset]. The reflectivity minimum at  $k \sim 557$   $\text{cm}^{-3}$  ( $f_p=1.67 \times 10^{13}$  Hz) is due to resonant absorption at the plasma frequency. From this we calculate a bulk carrier density  $n = 3.68 \times 10^{17}$   $\text{cm}^{-3}$  using the standard formula  $\omega_p^2 = ne^2/\epsilon m^*$  [41] where  $\omega_p = 2\pi f_p$ ,  $e$  is the electron charge,  $\epsilon(\omega_p) = 30\epsilon_0$  is the reported electric permittivity at the plasma frequency [41],  $\epsilon_0$  is the permittivity of free space and  $m^* \sim 0.14m_e$  [43] is the average effective mass of the bulk conduction band.

The SHG experimental layout is shown schematically in Fig.5. Ultrashort laser pulses with a center wavelength of 795 nm ( $\hbar\omega = 1.56$  eV) and a duration of 80 fs at FWHM were generated from a Ti:sapphire oscillator. The 80 MHz repetition rate was reduced to 1.6 MHz by a pulse picker and the average laser intensity of 0.63



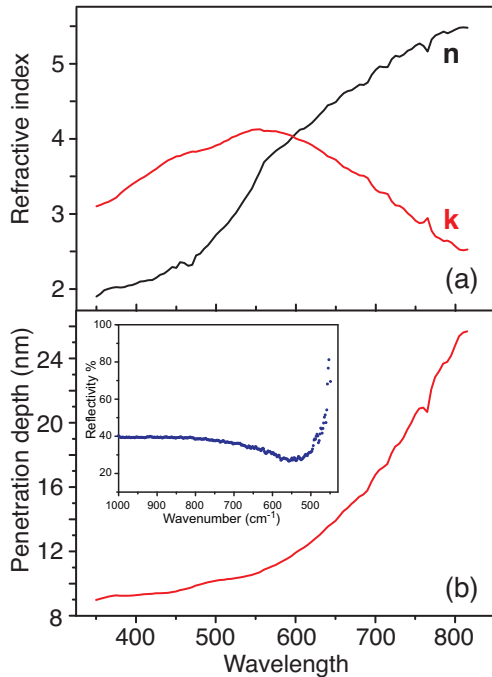


FIG. 4: (a) Real and imaginary parts of the  $\text{Bi}_2\text{Se}_3$  index of refraction as a function of light wavelength acquired by performing spectroscopic ellipsometry measurements. (b) Optical penetration depth as a function of wavelength. Inset: Measured FTIR reflectivity as a function of wavenumber normalized to the reflectivity of gold.

$\text{kW}/\text{cm}^2$  used for the experiments is well below the experimentally determined  $\text{Bi}_2\text{Se}_3$  damage threshold. The incident laser polarization was set by adjusting a  $\lambda/2$  and a  $\lambda/4$  waveplate. The beam was focused to a  $20 \mu\text{m}$   $1/e^2$  spot size on the sample at an incident angle of  $45^\circ$ . Specularly reflected photons at the second harmonic energy ( $\hbar 2\omega = 3.12 \text{ eV}$ ) with polarization in ( $P$ ) and out of ( $S$ ) the scattering plane were spatially separated by a polarizing beam splitting cube and simultaneously measured using calibrated photomultiplier tubes sensitive to  $3.1 \text{ eV}$  photons. Before the photomultiplier tubes, the reflected fundamental light was removed through both absorptive and interference filtering. The second harmonic nature of the detected signal was confirmed by checking that it scaled quadratically with the incident beam intensity [Fig.5 inset]. Part of the incident beam was split off before the sample and passed through a  $\beta$ -barium borate crystal to generate second harmonic light against which both  $P$  and  $S$  channels were normalized to account for laser intensity fluctuations.  $\text{Bi}_2\text{Se}_3(111)$  samples were mounted on a rotation stage and aligned so that the center of rotation coincided with the center of the focus of the incident beam. An accurate alignment was achieved by imaging the sample with a  $50\times$  microscope objective and a high resolution CCD camera. The second harmonic light generated as a function of the in-plane crystal orientation was measured by recording  $I(2\omega)$  in both po-

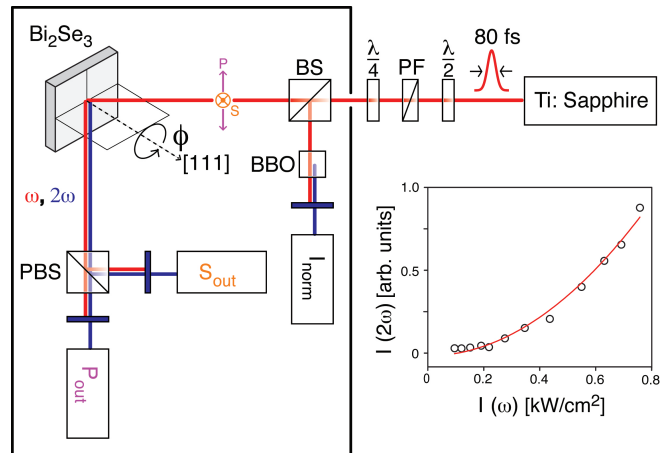


FIG. 5: Schematic of the experimental layout showing the complete beam path. The path of the fundamental ( $\omega$ ) and second harmonic ( $2\omega$ ) beams are shown in red and blue respectively. Experiments were performed in a dark enclosure to avoid stray light (see contour). Optical elements are denoted as follows: polarizing beam splitter (PBS), quarter- and half-wave plate ( $\lambda/4$  and  $\lambda/2$ ), beam splitter (BS), polarization filter (PF) and  $\beta$ -barium borate (BBO). Photomultiplier tubes are drawn as rectangles that measure the outgoing SHG with  $P_{out}$  and  $S_{out}$  polarizations as labeled. The photomultiplier tube used to measure laser intensity fluctuations is labeled  $I_{norm}$ . Wavelength filters are drawn as flat blue strips. Inset: Measured SHG intensity at  $\phi = 0$  in the  $P_{in} - P_{out}$  polarization geometry as a function of the fundamental light intensity. The red line is a fit that shows the expected quadratic relationship between the two.

larization channels as a function of the sample rotation angle  $\phi$  around the (111) axis, and as a function of the incident polarization [Fig.6(a)]. All samples were cleaved along the (111) plane in air or  $\text{O}_2$  at room temperature prior to measurement. For the  $\text{O}_2$  measurements, a continuous flow of  $\text{O}_2$  (99.5% Airgas) gas was directed on the sample at a pressure of 10 psi and at a distance of approximately 1 cm inside a sealed enclosure.

## B. First-order linear optical response

Before performing SHG measurements, we characterized the  $\chi^{(1)}$  first-order linear optical response by measuring the reflected light intensity at the fundamental frequency 200 minutes after the sample was cleaved in air. A typical trace is shown in the top panel of Fig. 6(b) for the  $P_{in} - P_{out}$  geometry. As a function of the sample rotation angle  $\phi$ ,  $I(\omega)$  is clearly isotropic, confirming that all off-diagonal tensor elements of  $\chi^{(1)}$  are zero and that  $\chi_{11}^{(1)} = \chi_{22}^{(1)}$  as expected from eq.(3). Similar isotropic traces were recorded for all input-output polarization geometries.

In section III.C we show that  $I(2\omega)$  increases after cleaving in air on the hour time scale before saturat-

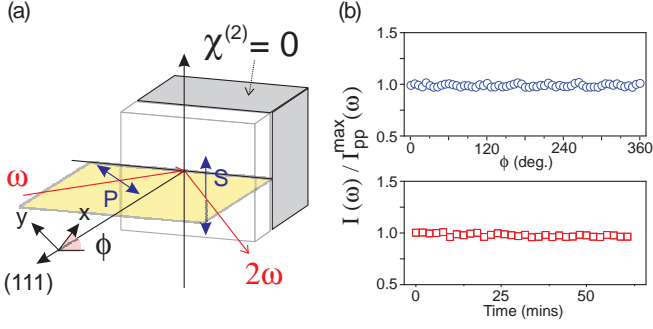


FIG. 6: (a) Schematic of the SHG experimental geometry. Surface and bulk regions are colored white and gray respectively (panel reprinted from [29]). (b) Top panel: Normalized intensity of the reflected beam at the fundamental frequency  $I(\omega)$  from the (111) surface of  $\text{Bi}_2\text{Se}_3$  measured as a function of azimuthal angle  $\phi$ . Data are shown in the  $P_{in} - P_{out}$  polarization geometry, but similar isotropic patterns were obtained under all four linear and four circular polarization geometries. Bottom panel: Intensity  $I(\omega)$  at  $\phi = 0^\circ$  in the  $P_{in} - P_{out}$  polarization geometry measured as a function of time after cleavage in air.

ing. To check that this is not related to a change in the bulk electronic structure or bulk doping, we measured the time dependence of  $I(\omega)$  immediately after cleaving in the  $P_{in} - P_{out}$  geometry, since the linear response is predominantly representative of bulk properties. It is clear from the bottom panel of Fig.6(b) that after cleaving the intensity of  $I(\omega)$  remains constant out to at least 60 minutes. No measurable changes in  $I(\omega)$  with time were observed at all  $\phi$  and in all input-output polarization geometries.

### C. Second-order nonlinear optical response

We now move on to characterize the second-order nonlinear optical response by measuring the second harmonic light generated from  $\text{Bi}_2\text{Se}_3$  (111). Equations (7)-(8) show that the tensor components of the combined  $\chi^{(2)} + \chi^{(3)}\mathcal{E}$  susceptibilities, which encode the surface plus accumulation region electrical responses respectively, can be determined by measuring  $I(2\omega)$  as a function of the sample rotation angle  $\phi$  in different input-output light polarization geometries. Figure 7(a)-(d) show the results of these measurements taken with linearly polarized light 200 minutes after the sample was cleaved in air. Unlike the first-order optical response [Fig.6(b)],  $I(2\omega)$  is clearly anisotropic as a function of  $\phi$  in all four linear polarization geometries. A simultaneous fit of eqs.(7)-(8) to the SHG patterns (including those taken with circularly polarized light in Fig.10) using a single set of susceptibility tensor elements yields excellent agreement [Fig.7(a)-(d)], which shows that the data are consistent with surface plus accumulation layer SHG from  $\text{Bi}_2\text{Se}_3$ . From the fit results we determine the relative magnitudes of  $|c^{(n)}|$ :

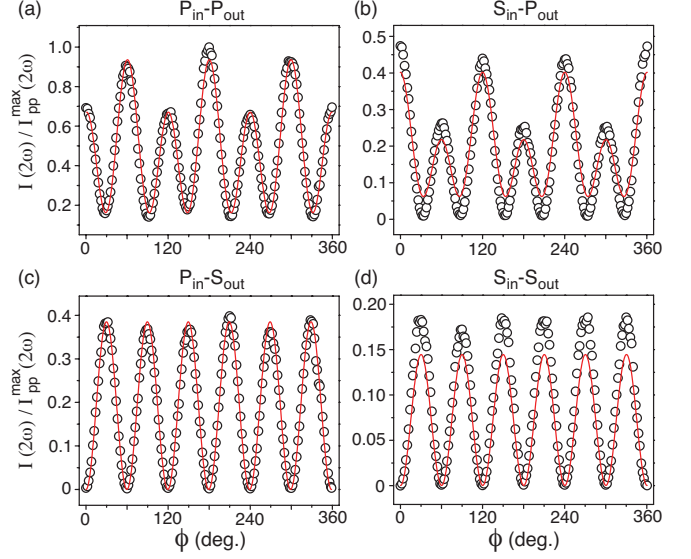


FIG. 7: Normalized SHG intensity  $I(2\omega)$  from the  $\text{Bi}_2\text{Se}_3$ (111) surface measured as a function of azimuthal angle  $\phi$  between the bisectrix  $(11\bar{2})$  and the scattering plane. Measurements taken 200 minutes after cleavage in (a)  $P_{in} - P_{out}$ , (b)  $S_{in} - P_{out}$ , (c)  $P_{in} - S_{out}$  and (d)  $S_{in} - S_{out}$  incident and outgoing photon polarization geometries. All data sets are normalized to the maximum intensity measured at  $t = 200$  mins in the  $P_{in} - P_{out}$  geometry. Solid lines are fits to eq. (7).

$$\begin{aligned} |c^{(1)}| &= 1 \\ |c^{(2)}| &= 1.31 \\ |c^{(3)}| &= 0.19 \\ |c^{(4)}| &= 8.99 \end{aligned}$$

(11)

where each  $|c^{(n)}|$  is normalized to  $|c^{(1)}|$ . Because the phase of the complex fit parameters cannot be uniquely determined, it is only informative to show the absolute values. We find that the largest contribution to the combined  $\chi^{(2)} + \chi^{(3)}\mathcal{E}$  nonlinear susceptibility comes from  $|c^{(4)}|$ , which describes the only purely out-of-plane electrical response at the surface [eqs.(9)-(10)]. In section III.D we show that the relative contributions of surface ( $\chi^{(2)}$ ) and accumulation region ( $\chi^{(3)}\mathcal{E}$ ) SHG can be determined by studying the time evolution of  $I(2\omega)$  after cleaving the sample.

The data in Fig.7 exhibit a clear 3-fold or 6-fold rotational symmetry depending on whether the outgoing photons measured have a polarization component perpendicular ( $P$ -polarized) or parallel ( $S$ -polarized) to the sample plane respectively. Because  $S$ -polarized light only has in-plane electric-field components, it is primarily a sensitive measure of the in-plane response. This likely originates from the anharmonic polarizability of the Se-Se bonds [Fig.1], which have a 6-fold symmetric arrange-



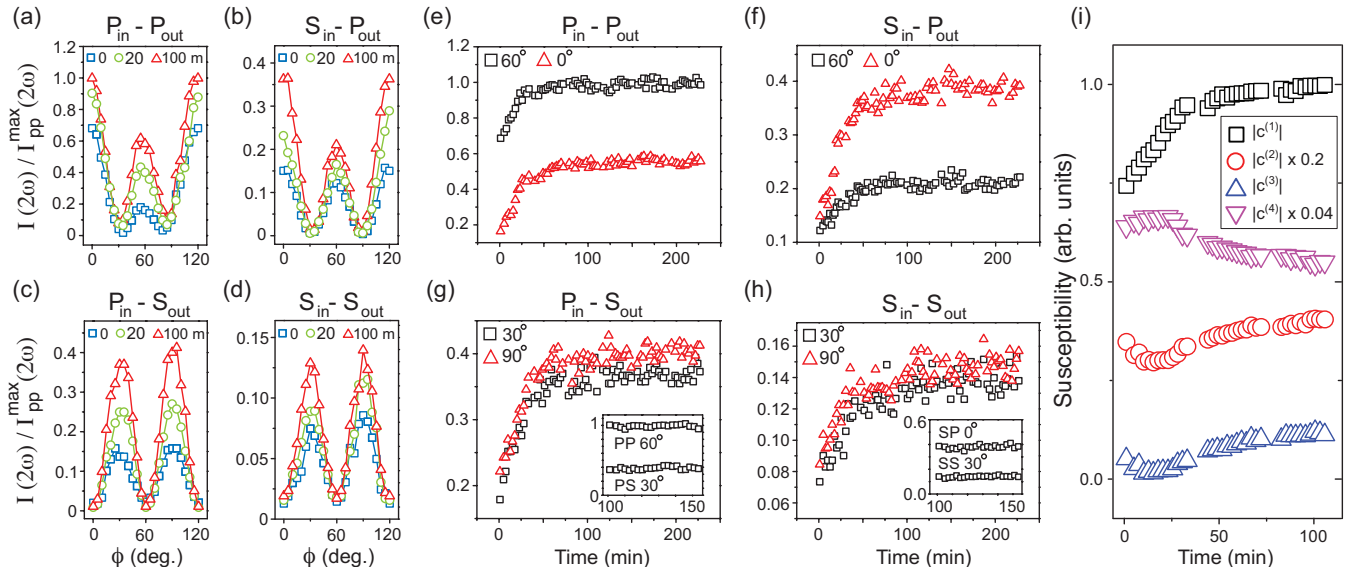


FIG. 8:  $\phi$  dependence of the normalized SHG intensity as a function of time after cleavage in air in the (a)  $P_{in}-P_{out}$ , (b)  $S_{in}-P_{out}$ , (c)  $P_{in}-S_{out}$  and (d)  $S_{in}-S_{out}$  photon polarization geometries. (e)-(h) Accompanying detailed time dependence along high crystal symmetry directions (panels reprinted from [29]). The insets in (g) and (h) show the time evolution of the peak SHG intensities starting at 100 minutes after cleavage in air, prior to which the sample was not exposed to laser light. (i) Fit coefficients from fitting eq.(7) to the SHG data as a function of time after cleavage in air. The gaps in the data at approximately 5, 40 and 75 minutes are where full  $\phi=0^\circ$  to  $\phi=360^\circ$  traces were taken to confirm that rotational symmetry was maintained as a function of time.

ment in the sample plane. On the other hand, because  $P$ -polarized light contains an electric-field component along  $\hat{z}$ , it is sensitive to the out-of-plane response originating from the Se-Bi bonds, which have a 3-fold symmetric arrangement that extend into the bulk.

#### D. Surface molecular doping effects on SHG

To prove that the surface and accumulation region SHG is dominant over multipole bulk effects, and to quantify their relative contributions, we studied the effects of changing the surface carrier concentration. Angle-resolved photoemission spectroscopy (ARPES) studies have shown that  $\text{Bi}_2\text{Se}_3$  exhibits an intrinsic surface band-bending after cleavage in ultra-high vacuum (UHV) that acts to monotonically increase the electron density at the surface on the hour time scale until a stable accumulation layer is formed [8, 17, 44]. If SHG from  $\text{Bi}_2\text{Se}_3$  is in fact surface sensitive, such a surface electronic change should be manifested in our measurements. This is because, as shown in section II.A, the band-bending induced electric field acts to break inversion symmetry over the depth that it penetrates into the bulk [Fig.2], thereby permitting SHG in the accumulation region with an intensity that is proportional to the field strength. Figure 8(a)-(d) show a clear increase in  $I(2\omega)$  at all  $\phi$  and in all input-output linear polariza-

tion geometries as a function of time after cleavage in air. However, there is no change in the rotational symmetry of the SHG patterns, which rules out any trigonal symmetry breaking atomic reconstruction, as is typical of semiconductors such as Si(111) in air [31]. Figure 8(e)-(h) show the complete time dependencies of the SHG peak intensities, which all undergo the same monotonic increase by as much as 400% within 50 minutes following cleavage, after which they saturate to a value that remains constant out to at least 600 mins. This is a trend highly consistent with the time evolution of the surface Fermi level observed using ARPES [8] and cannot have a bulk origin as no bulk electronic changes were observed with time after cleaving [Fig.6(b)].

Slow photo-induced changes in SHG intensity are known to occur on semiconductor surfaces such as GaAs [45] and oxidized Si [34, 46] through a two-step charge-excitation charge-trapping processes [34, 45]. To test for such effects, we repeated the measurements after keeping the sample unexposed to laser light for the first 100 mins after cleavage [Fig.8 (g)-(h) insets]. The fact that the SHG intensities under these conditions show no time dependence and match the previous saturation intensities shows that the observed time evolution is purely a surface doping effect and not a photo-induced effect.

To understand how the nonlinear susceptibilities evolve with time, we simultaneously fit the SHG data in Fig.8(e)-(h) at each point in time to eq.(7). The time

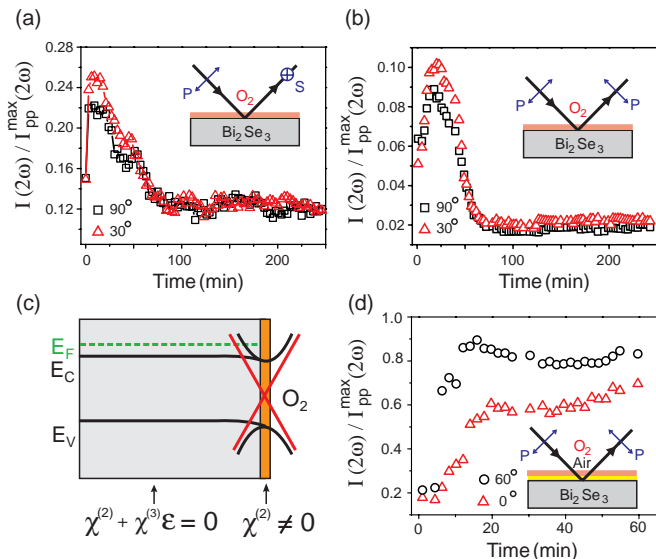


FIG. 9: (a) Time dependence of the SHG peak intensities measured in the  $P_{in}-S_{out}$  polarization geometry after cleaving in O<sub>2</sub> (panel reprinted from [29]). (b) Time dependence of the SHG minima measured in the  $P_{in}-P_{out}$  polarization geometry after cleaving in O<sub>2</sub>. Similar behaviors were also observed in other polarization geometries. (c) Schematic of the energy evolution of the bulk conduction band minimum ( $E_C$ ) and bulk valence band maximum ( $E_V$ ) relative to the Fermi level ( $E_F$ ) as a function of distance to the O<sub>2</sub> covered surface. (d) Time dependence of the SHG peak intensities measured in the  $P_{in}-P_{out}$  polarization geometry after cleaving in air then immediately covering the surface with O<sub>2</sub> gas.

dependence of the fit coefficients is shown in Fig.8(i). We find that  $|c^{(1)}|$ ,  $|c^{(2)}|$  and  $|c^{(3)}|$ , which together primarily encode the in-plane electrical response [eqs. (9)-(10)], generally increase as a function of time. This precludes a change of the inter-atomic layer distance at the surface after cleaving as the primary source of the increased SHG signal because this would predominantly only affect the out-of-plane susceptibilities. The coefficient  $|c^{(4)}|$ , which describes the only purely out-of-plane electrical response, on the other hand generally decreases as a function of time. The dip feature exhibited by  $|c^{(2)}|$ ,  $|c^{(3)}|$  and  $|c^{(4)}|$  at early times is currently unclear and requires and awaits a detailed microscopic theoretical description of SHG from Bi<sub>2</sub>Se<sub>3</sub>. However, we note that this feature is similar to that observed in the raw SHG data for samples cleaved in an O<sub>2</sub> environment as a function of time in Fig.9(a)-(b).

Because we find that the band-bending in air occurs on the same time scale observed in samples cleaved in UHV, its cause is unlikely related to the direct charging of the surface by adsorbed molecules from the environment, for the adsorption rates in air and UHV will be different by orders of magnitude. An alternative possibility is that it is due to an intrinsic material property. Intrinsic band-bending is known to occur through the migration of charged impurities within the crystal—a process

that can take place on the hour time scale [48]. If this is the case in our samples, the migrating impurities are most likely negatively charged Se vacancies, which are prolific in Bi<sub>2</sub>Se<sub>3</sub> [41], that may move to the surface to lower the surface energy of the topmost Se layer after cleaving, thereby increasing the surface carrier density.

Although we have shown that the  $\chi^{(2)}$  and  $\chi^{(3)}\mathcal{E}$  contributions to SHG from Bi<sub>2</sub>Se<sub>3</sub>(111) can be distinguished, isolating the surface electrical response, which is only encoded in  $\chi^{(2)}$ , will require eliminating the accumulation region SHG. Experiments have shown that O<sub>2</sub> is an effective electron acceptor when deposited on the surface of Bi<sub>2</sub>Se<sub>3</sub> [49]. To demonstrate that the accumulation region SHG can be eliminated and to confirm that SHG is sensitive to tuning the surface carrier density, we studied the time evolution of  $I(2\omega)$  after cleaving the sample in an O<sub>2</sub> environment. Figure 9(a)-(b) show that  $I(2\omega)$  initially increases to reach approximately 50% of the saturation intensity value in air, then slowly decreases back to its initial value. These results show that electron transfer from the Bi<sub>2</sub>Se<sub>3</sub> surface to the adsorbed O<sub>2</sub> molecules takes place only after some finite surface charge has developed, and that O<sub>2</sub> can restore the surface back to an un-charged state, where  $\mathcal{E}=0$ , but cannot hole dope beyond this state [Fig.9(c)]. Figure 9(d) shows that this hole doping does not occur when the sample is cleaved in air then immediately exposed to O<sub>2</sub>, indicating that the charge transfer only occurs by molecules initially adsorbed on the surface.

Assuming that the surface doping is negligibly small immediately after cleaving in air ( $\mathcal{E} \sim 0$ ), we estimate that the  $\chi^{(2)}$  and  $\chi^{(3)}\mathcal{E}$  contributions to SHG are roughly equal at long times after cleaving in air. We estimate that the accumulation region penetrates approximately 12 nm into the bulk using the Thomas-Fermi screening length  $\lambda_{TF} = (3ne^2/2\epsilon_{dc}E_f)^{-1/2}$  [47] as an approximation, where  $n = 3.68 \times 10^{17} \text{ cm}^{-3}$  is the bulk carrier density [Fig.4(b) inset],  $\epsilon_{dc} \sim 113\epsilon_0$  is the  $dc$  electric permittivity for Bi<sub>2</sub>Se<sub>3</sub> [43], and we approximate  $E_f = \frac{\hbar^2}{2m^*} (3\pi^2 n)^{2/3} = .013 \text{ eV}$  using  $m^* = 0.14m_e$  [43].

## E. Circular Dichroism SHG

Having established that a pure surface  $\chi^{(2)}$  measurement can be performed on the Bi<sub>2</sub>Se<sub>3</sub> materials class that is sensitive to both the surface crystal structure and the surface carrier concentration, we consider how SHG can be used to monitor time-reversal symmetry (TRS) at a topological insulator surface. It has been proposed that new TRS broken phases can be measured through the differential absorption of right-( $R$ ) versus left-( $L$ ) circularly polarized light [14, 22, 23]. In order to understand whether second harmonic versions of such experiments are feasible, it is necessary to measure the intrinsic second-order optical response of Bi<sub>2</sub>Se<sub>3</sub> to circularly polarized light.

Second harmonic circular dichroism (CD), the differ-

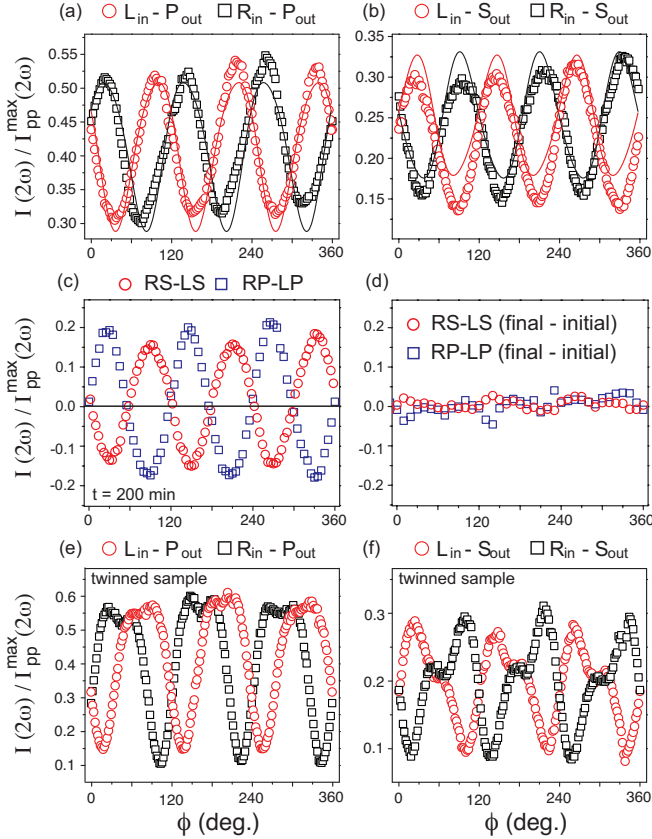


FIG. 10: Normalized  $\phi$ -dependent SHG intensity patterns from  $\text{Bi}_2\text{Se}_3$  measured 200 minutes after cleavage in air under (a) left-circular in ( $L_{in}$ )  $P_{out}$  and right-circular in ( $R_{in}$ )  $P_{out}$ , and (b)  $L_{in}$ - $S_{out}$  and  $R_{in}$ - $S_{out}$  photon polarization geometries. Solid lines are theoretical fits to eq.(7). (c) Circular dichroism ( $I_R - I_L$ ) corresponding to data in panels (a) and (b). (d) Difference between circular dichroism measured at 200 minutes after cleavage and immediately after cleavage (panels (c)-(d) reprinted from [29]). Normalized SHG intensity patterns from a different sample batch that are likely crystal twinned in (e) left-circular in ( $L_{in}$ )  $P_{out}$  and right-circular in ( $R_{in}$ )  $P_{out}$ , and (f)  $L_{in}$ - $S_{out}$  and  $R_{in}$ - $S_{out}$  photon polarization geometries.

ence in SHG yield using incident  $R$ - versus  $L$ -circularly polarized fundamental light, was measured from  $\text{Bi}_2\text{Se}_3$  200 minutes after cleavage in air. Figure 10(a)-(b) show a clear difference between the SHG intensity patterns measured using  $R$ - versus  $L$ -circularly polarized input for both  $S$ - and  $P$ -polarized output geometries, which are well described by eq. (8) using the same set of susceptibility values fitted to Fig.7(a)-(d). By plotting CD as a function of  $\phi$  [Fig.10(c)], we find that CD varies sinusoidally, with the  $S$ - and  $P$ -polarized output components out of phase by exactly  $180^\circ$ . Although second harmonic CD can arise through the interference of higher-order bulk multipole and surface dipole SHG radiation, such effects are known to be suppressed when the photon energy exceeds the bulk band gap [35] and we have

shown that the bulk multipole contributions to SHG are negligible. Equation (8) shows that that CD SHG can be generated by the surface alone.

While CD is generally non-zero, Fig.10(c) shows that it vanishes when  $\phi$  is an integer multiple of  $60^\circ$ , angles where the scattering plane coincides with a mirror plane of the (111) surface [Fig.1]. Such zeroes are protected by mirror symmetry because  $R$ - and  $L$ -circularly polarized light transform into one another under mirror reflection about the scattering plane. Because a magnetization can break mirror symmetry, measuring departures from zero in CD along these specific values of  $\phi$  can be a sensitive probe of TRS breaking on the surface of  $\text{Bi}_2\text{Se}_3$ . Remarkably, we find that CD at a general  $\phi$  is insensitive to surface charging, as evidenced by the lack of measurable change as a function of time after cleavage [Fig.10(d)]. This suggests that sensitive searches for TRS breaking induced CD may be carried out without the need for careful control of surface charging, which is an important and robust way of studying the physics of surface doped topological insulators or buried interfaces between topological insulators and ordinary materials [1, 2]. We are currently investigating why CD is insensitive to surface charging.

In certain samples, the  $\phi$ -dependence of  $I(2\omega)$  with circularly polarized light exhibited additional features that cannot be accounted for by eq.(8) [Fig.10(e)-(f)]. These appear to be smaller SHG extrema that are shifted from the extrema exhibited in Fig.10(a)-(b) by  $60^\circ$ . However, the  $\phi$ -dependence of  $I(2\omega)$  in the linear polarization input configurations in the same samples appeared to be unaffected due to the  $60^\circ$  periodicity of the SHG extrema. The origin of these features is likely due to crystal twinning and further confirmation is underway.

#### IV. SUMMARY AND OUTLOOK

We have presented a theoretical and experimental study of second harmonic generation from the topological insulator  $\text{Bi}_2\text{Se}_3$ . By performing a crystal symmetry analysis we identified the nonlinear electric susceptibility tensor elements that contribute to SHG. The analysis showed that the process is forbidden in the bulk of  $\text{Bi}_2\text{Se}_3$  owing to the presence of inversion symmetry, but can be generated at the surface where inversion symmetry is necessarily broken. We also found that SHG can be generated near the surface in the accumulation region where the band-bending electric field breaks inversion symmetry over the depth that it penetrates into the bulk. We incorporated the symmetry analysis results into a phenomenological model and showed that the relative magnitudes of the susceptibility tensor elements can be determined by measuring the SHG intensity and polarization as a function of the in-plane crystal orientation and incident laser polarization.

To test the model, we performed SHG experiments on bulk single crystals of  $\text{Bi}_2\text{Se}_3$ . We first described the sample growth process and reported the characterization results. We also determined the complex index of refraction in the visible range, which is a necessary input parameter to the theoretical model, by performing spectroscopic ellipsometry measurements. We described the experiment we designed to isolate the SHG signal and characterized the first-order linear optical response. We measured the radiated SHG intensity and polarization as a function of crystal orientation and incident laser polarization, and the results are consistent with our theoretical model. We fit the data and reported the relative contributions to SHG from each of the nonlinear susceptibility elements.

To confirm that the surface and accumulation region are the dominant source of SHG and to quantify their relative contributions, we performed a surface doping dependence study. When the sample was cleaved in air, the SHG intensity in all polarization configurations monotonically increased on the hour time scale before saturating and remaining constant out to at least several hours. We attributed this behavior to the slow formation of the SHG generating accumulation region that results from the intrinsic band-bending in  $\text{Bi}_2\text{Se}_3$  after cleaving [8, 17]. We estimated from the results that the surface and accumulation region contributions to SHG were comparable at long times in air. When cleaved in an oxygen environment, the SHG intensity initially increased then slowly decreased back to its initial value. This is consistent with ARPES results showing that depositing oxygen on the surface of  $\text{Bi}_2\text{Se}_3$  lowers the surface carrier density and hence the magnitude of the band-bending electric field that induces SHG in the accumulation region [49]. These results show that SHG can be used to monitor changes in the surface Fermi level.

We finally investigated the SHG response using circularly polarized light as a function of the in-plane crystal orientation. We found pronounced circular dichroism at all crystal rotation angles except along planes of crystal mirror symmetry where the circular dichroism vanished. We proposed that sensitive searches for time-reversal symmetry breaking could be performed by monitoring the SHG circular dichroism along these mirror planes.

The theoretical description and experimental realization of surface second harmonic generation from the  $\text{Bi}_2\text{Se}_3$  materials class provides a novel contact-free probe of the electrical response from a single surface of a topological insulator. The ability to perform such surface sensitive experiments with tuning control of the surface carrier concentration in ambient conditions is promising for future technological applications of topological insulators.

## V. APPENDIX

### A. Symmetry analysis of tensor components

Similar to the procedure used to find the  $\chi^{(1)}$  components, the non-vanishing  $\chi^{(2)}$  tensor elements can be found by transforming  $\chi^{(2)}$  under the  $C_{3v}$  rotation and mirror symmetry operations [Fig.1] via eq.(2) and equating the resulting tensors. We find that  $\chi^{(2)}$  assumes the form [31]

$$\chi^{(2)} = \begin{pmatrix} \begin{pmatrix} \chi_{xxx} \\ 0 \\ \chi_{xxz} \end{pmatrix} & \begin{pmatrix} 0 \\ -\chi_{xxx} \\ 0 \end{pmatrix} & \begin{pmatrix} \chi_{xxz} \\ 0 \\ 0 \end{pmatrix} \\ \begin{pmatrix} 0 \\ -\chi_{xxx} \\ 0 \end{pmatrix} & \begin{pmatrix} -\chi_{xxx} \\ 0 \\ \chi_{xxz} \end{pmatrix} & \begin{pmatrix} 0 \\ \chi_{xxz} \\ 0 \end{pmatrix} \\ \begin{pmatrix} \chi_{zxx} \\ 0 \\ 0 \end{pmatrix} & \begin{pmatrix} 0 \\ \chi_{zxx} \\ 0 \end{pmatrix} & \begin{pmatrix} 0 \\ 0 \\ \chi_{zzz} \end{pmatrix} \end{pmatrix}$$

which contains four non-zero independent components:  $\chi_{xxx}$  ( $=-\chi_{xyy} = -\chi_{yxy}$ ),  $\chi_{zxx}$  ( $=\chi_{zyy}$ ),  $\chi_{xxz}$  ( $=\chi_{yyz}$ ), and  $\chi_{zzz}$ , and  $x$ ,  $y$  and  $z$  refer to the crystal coordinates defined in Fig.1. Here we choose the tensor representation where the index  $i$  represents the row,  $j$  the column, and  $k$  the row within each  $ij$  element. Since we perform experiments by rotating a sample about its (111) axis, we transform  $\chi^{(2)}$  from the sample coordinate frame to the laboratory coordinate frame using eq.(2) with  $T$  substituted by the rotation matrix [31]

$$R(\phi) = \begin{pmatrix} \cos(\phi) & -\sin(\phi) & 0 \\ \sin(\phi) & \cos(\phi) & 0 \\ 0 & 0 & 1 \end{pmatrix}$$

This yields [31]

$$\chi^{(2)} \rightarrow \begin{pmatrix} \begin{pmatrix} \chi_{xxx} \cos(3\phi) \\ -\chi_{xxx} \sin(3\phi) \\ \chi_{xxz} \end{pmatrix} & \begin{pmatrix} -\chi_{xxx} \sin(3\phi) \\ -\chi_{xxx} \cos(3\phi) \\ 0 \end{pmatrix} & \begin{pmatrix} \chi_{xxz} \\ 0 \\ 0 \end{pmatrix} \\ \begin{pmatrix} -\chi_{xxx} \sin(3\phi) \\ -\chi_{xxx} \cos(3\phi) \\ 0 \end{pmatrix} & \begin{pmatrix} -\chi_{xxx} \cos(3\phi) \\ \chi_{xxx} \sin(3\phi) \\ \chi_{xxz} \end{pmatrix} & \begin{pmatrix} 0 \\ \chi_{xxz} \\ 0 \end{pmatrix} \\ \begin{pmatrix} \chi_{zxx} \\ 0 \\ 0 \end{pmatrix} & \begin{pmatrix} 0 \\ \chi_{zxx} \\ 0 \end{pmatrix} & \begin{pmatrix} 0 \\ 0 \\ \chi_{zzz} \end{pmatrix} \end{pmatrix}$$

We now impose the same symmetry conditions on  $\chi^{(3)}$  as was done above for  $\chi^{(2)}$ . Unlike odd rank tensors, all components of even rank tensors do not necessarily vanish under inversion symmetry. Therefore, the  $\chi^{(3)}$  contribution to SHG does not necessarily vanish in the bulk. However, SHG will only be generated by  $\chi^{(3)}$  over the finite accumulation region that the band-bending field  $\vec{\mathcal{E}}$  penetrates into the bulk. In general  $\chi^{(3)}$  has 81 components. Under the transformations by the symmetry operations of  $D_{3d}^5$ , this is reduced to the following form

$$\chi^{(3)} = \begin{pmatrix} \chi_{11}^{(3)} & \chi_{12}^{(3)} & \chi_{13}^{(3)} \\ \chi_{21}^{(3)} & \chi_{22}^{(3)} & \chi_{23}^{(3)} \\ \chi_{31}^{(3)} & \chi_{32}^{(3)} & \chi_{33}^{(3)} \end{pmatrix}$$

where [51]

$$\chi_{11}^{(3)} = \begin{pmatrix} \chi_{xxxx} & 0 & -\chi_{xyyz} \\ 0 & \chi_{xxyy} & 0 \\ -\chi_{xyzy} & 0 & \chi_{xxzz} \end{pmatrix}$$

$$\chi_{12}^{(3)} = \begin{pmatrix} 0 & \chi_{xyxy} & 0 \\ \chi_{xxxx} - \chi_{xxyy} - \chi_{xyxy} & 0 & \chi_{xyyz} \\ 0 & \chi_{xyzy} & 0 \end{pmatrix}$$

$$\chi_{13}^{(3)} = \begin{pmatrix} -\chi_{xzyy} & 0 & \chi_{xzxx} \\ 0 & \chi_{xzyy} & 0 \\ \chi_{xzxx} & 0 & 0 \end{pmatrix}$$

$$\chi_{21}^{(3)} = \begin{pmatrix} 0 & \chi_{xxxx} - \chi_{xxyy} - \chi_{xyxy} & 0 \\ \chi_{xyxy} & 0 & \chi_{xyyz} \\ 0 & \chi_{xyzy} & 0 \end{pmatrix}$$

$$\chi_{22}^{(3)} = \begin{pmatrix} \chi_{xxyy} & 0 & \chi_{xyyz} \\ 0 & \chi_{xxxx} & 0 \\ \chi_{xyzy} & 0 & \chi_{xxzz} \end{pmatrix}$$

$$\chi_{23}^{(3)} = \begin{pmatrix} 0 & \chi_{xzyy} & 0 \\ \chi_{xzyy} & 0 & \chi_{xzxx} \\ 0 & \chi_{xzxx} & 0 \end{pmatrix}$$

$$\chi_{31}^{(3)} = \begin{pmatrix} -\chi_{xzyy} & 0 & \chi_{xzxx} \\ 0 & \chi_{xzyy} & 0 \\ \chi_{xzxx} & 0 & 0 \end{pmatrix}$$

$$\chi_{32}^{(3)} = \begin{pmatrix} 0 & \chi_{xzyy} & 0 \\ \chi_{xzyy} & 0 & \chi_{xzxx} \\ 0 & \chi_{xzxx} & 0 \end{pmatrix}$$

$$\chi_{33}^{(3)} = \begin{pmatrix} \chi_{zzxx} & 0 & 0 \\ 0 & \chi_{zzxx} & 0 \\ 0 & 0 & \chi_{zzzz} \end{pmatrix}$$

which contains 17 independent components [50]. In the laboratory coordinate frame,  $\chi^{(3)}$  transforms according to [51]

$$\chi_{11}^{(3)} \rightarrow$$

$$\begin{pmatrix} \chi_{xxxx} & 0 & -\chi_{xyyz} \cos(3\phi) \\ 0 & \chi_{xxyy} & -\chi_{xyyz} \sin(3\phi) \\ -\chi_{xyzy} \cos(3\phi) & -\chi_{xyzy} \sin(3\phi) & \chi_{xxzz} \end{pmatrix}$$

$$\chi_{12}^{(3)} \rightarrow$$

$$\begin{pmatrix} 0 & \chi_{xyxy} & -\chi_{xyyz} \sin(3\phi) \\ \chi_{xxxx} - \chi_{xxyy} - \chi_{xyxy} & 0 & \chi_{xyyz} \cos(3\phi) \\ -\chi_{xyzy} \sin(3\phi) & \chi_{xyzy} \cos(3\phi) & 0 \end{pmatrix}$$

$$\chi_{13}^{(3)} \rightarrow \begin{pmatrix} -\chi_{xzyy} \cos(3\phi) & -\chi_{xzyy} \sin(3\phi) & \chi_{xzxx} \\ -\chi_{xzyy} \sin(3\phi) & \chi_{xzyy} \cos(3\phi) & 0 \\ \chi_{xzxx} & 0 & 0 \end{pmatrix}$$

$$\chi_{21}^{(3)} \rightarrow$$

$$\begin{pmatrix} 0 & \chi_{xxxx} - \chi_{xxyy} - \chi_{xyxy} & -\chi_{xyyz} \sin(3\phi) \\ \chi_{xyxy} & 0 & \chi_{xyyz} \cos(3\phi) \\ -\chi_{xyzy} \sin(3\phi) & \chi_{xyzy} \cos(3\phi) & 0 \end{pmatrix}$$

$$\chi_{22}^{(3)} \rightarrow \begin{pmatrix} \chi_{xxyy} & 0 & \chi_{xyyz} \cos(3\phi) \\ 0 & \chi_{xxxx} & \chi_{xyyz} \sin(3\phi) \\ \chi_{xyzy} \cos(3\phi) & \chi_{xyzy} \sin(3\phi) & \chi_{xxxx} \end{pmatrix}$$

$$\chi_{32}^{(3)} \rightarrow \begin{pmatrix} -\chi_{zxyy} \sin(3\phi) & \chi_{zxyy} \cos(3\phi) & 0 \\ \chi_{zxyy} \cos(3\phi) & \chi_{zxyy} \sin(3\phi) & \chi_{zzxz} \\ 0 & \chi_{zzxz} & 0 \end{pmatrix}$$

$$\chi_{23}^{(3)} \rightarrow \begin{pmatrix} -\chi_{xzyy} \sin(3\phi) & \chi_{xzyy} \cos(3\phi) & 0 \\ \chi_{xzyy} \cos(3\phi) & \chi_{xzyy} \sin(3\phi) & \chi_{zzxz} \\ 0 & \chi_{zzxz} & 0 \end{pmatrix}$$

$$\chi_{33}^{(3)} \rightarrow \begin{pmatrix} \chi_{zzxx} & 0 & 0 \\ 0 & \chi_{zzxx} & 0 \\ 0 & 0 & \chi_{zzzz} \end{pmatrix}$$

$$\chi_{31}^{(3)} \rightarrow \begin{pmatrix} -\chi_{zxyy} \cos(3\phi) & -\chi_{zxyy} \sin(3\phi) & \chi_{zzxz} \\ -\chi_{zxyy} \sin(3\phi) & \chi_{zxyy} \cos(3\phi) & 0 \\ \chi_{zzxz} & 0 & 0 \end{pmatrix}$$

- 
- [1] J. E. Moore, *Nature* **464**, 194 (2010).  
[2] M. Z. Hasan and C. L. Kane, *Rev. Mod. Phys.* **82**, 3045 (2010).  
[3] X.-L. Qi and S.-C. Zhang, *Phys. Today* **63**, 33 (2010).  
[4] D. Hsieh *et al.* *Nature* **452**, 970-974 (2008).  
[5] D. Hsieh *et al.* *Science* **323**, 919-922 (2009).  
[6] Y. Xia *et al.* *Nature Phys.* **5**, 398-402 (2009).  
[7] Y.L. Chen *et al.* *Science* **325**, 5937 (2009).  
[8] D. Hsieh *et al.* *Nature* **460**, 1101-1105 (2009).  
[9] P. Roushan *et al.* *Nature* **460**, 1106-1109 (2009).  
[10] Z. Alpichshev *et al.* *Phys. Rev. Lett.* **104**, 016401 (2010).  
[11] S. Raghu, S. B. Chung, X.-L. Qi and S.-C. Zhang, *Phys. Rev. Lett.* **104**, 116401 (2010).  
[12] P. Hosur, *Phys. Rev. B* **83**, 035309 (2011).  
[13] J.W. McIver, D. Hsieh, H. Steinberg, P. Jarillo-Herrero and N. Gedik, *Nature Nano.* **7**, 96-100 (2012).  
[14] X.-L. Qi, T. L. Hughes and S.-C. Zhang, *Phys. Rev. B* **78**, 195424 (2008).  
[15] G. Rosenberg and M. Franz, *Phys. Rev. B* **82**, 035105 (2010).  
[16] H. Zhang *et al.*, *Nature Phys.* **5**, 438 (2009).  
[17] D. Hsieh *et al.*, *Phys. Rev. Lett.* **103**, 146401 (2009).  
[18] J. G. Checkelsky, Y. S. Hor, R. J. Cava and N. P. Ong, *Phys. Rev. Lett.* **106** 196801 (2011).  
[19] H. Steinberg, D. R. Gardner, Y. S. Lee and P. Jarillo-Herrero, *Nano Lett.* (2010).  
[20] Y.S. Kim *et al.*, *Phys. Rev. B* **84** 073109 (2011).  
[21] L.A. Wray *et al.*, arXiv:1105.4794 (2011).  
[22] W.-K. Tse and A. H. MacDonald, *Phys. Rev. Lett.* **105**, 057401 (2010).  
[23] J. Maciejko, X.-L. Qi, H. Dennis Drew and S.-C. Zhang, *Phys. Rev. Lett.* **105**, 166803 (2010).  
[24] A. B. Sushkov *et al.*, *Phys. Rev. B* **82**, 125110 (2010) .  
[25] A. D. LaForge *et al.*, *Phys. Rev. B* **81**, 125120 (2010) .  
[26] N. P. Butch *et al.*, *Phys. Rev. B* **81**, 241301(R) (2010).  
[27] J.N. Hancock *et al.*, *Phys. Rev. Lett.* **107**, 136803 (2011)  
[28] R. Valdes Aguilar *et al.*, arXiv:1105.0237 (2011)  
[29] D. Hsieh, J.W. McIver, D.H. Torchinsky, D.R. Gardner, Y.S. Lee and N. Gedik., *Phys. Rev. Lett.* **106**, 057401 (2011).  
[30] D. Hsieh, F. Mahmood, J.W. McIver, D.R. Gardner, Y.S. Lee and N. Gedik. *Phys. Rev. Lett.* **107**, 077401 (2011)  
[31] Y. R. Shen, in *The principles of nonlinear optics*, (Wiley-Interscience, New York, 1984).  
[32] Birss, R.R. *Symmetry and Magnetism* (North-Holland Publishing Company, Amsterdam, 1964).  
[33] H.L. Dai & W. Ho. *Laser spectroscopy and photochemistry on metal surfaces* (World Scientific Publishing Co., Singapore, 1995).  
[34] J. Bloch, J. G. Mihaychuk and H. M. van Driel, *Phys. Rev. Lett.* **77**, 920 (1996).  
[35] F.-X. Wang *et al.*, *Phys. Rev. B* **80**, 233402 (2009).  
[36] Li, X. *et al.* Circular dichroism in second harmonic generation from oxidized Si(001). *Appl. Phys. Lett.* **89**, 022102 (2009).  
[37] V. Mizrahi and J. E. Sipe, *J. Opt. Soc. Am. B* **5** 660 (1988).  
[38] T.F. Heinz. *Nonlinear optics of surfaces and adsorbates* (Ph.D. Thesis, 1982).  
[39] Bloembergen, N., Pershan, P.S. Light waves at the boundary of nonlinear media. *Phys. Rev.* **128**, 606-622 (1962).  
[40] E. Hecht. *Optics, 3rd Edition.* Addison-Wesley. United States (1998). p. 111  
[41] A. Sklenar, C. Drasar, A. Krejcová and P. Lostak. *Cryst. Res. Technol.* **35**, 1069-1076 (2000).  
[42] H. Fujiwara. *Spectroscopic Ellipsometry: Principles and Applications.* John Wiley & Sons Inc. Chichester, England (2007). p. 23  
[43] J. G. Analytis *et al.*, *Phys. Rev. B* **81**, 205407 (2010).  
[44] M. Bianchi *et al.*, *Nature Communications* **1**, Article Number:128 (2010).  
[45] J. Qi, M. S. Yeganeh, I. Koltover, A. G. Yodh and W. M. Theis, *Phys. Rev. Lett.* **71**, 633 (1993).  
[46] S. A. Mitchell, T. R. Ward, D. D. M. Wayner and G. P. Lopinski, *J. Phys. Chem. B* **106**, 9873 (2002).  
[47] N.W. Ashcroft, N.D. Mermin, *Solid State Physics.* Thompson Learning, Inc. United States (1976). p. 342.  
[48] A. Sosin, *Phys. Rev.* **122**, 1112-1116 (1961).  
[49] Y. L. Chen *et al.*, *Science* **329**, 659 (2010).  
[50] S. V. Popov, Yu. P. Svirko and N. I. Zheludev. *Susceptibility tensors for nonlinear optics.* (IOP, London, 1995).  
[51] Boyd, R. *Nonlinear Optics, 3rd edition.* Elsevier. United States (2008).